JOURNAL OF THE ATMOSPHERIC SCIENCES

Dynamics of Subsiding Shells In Actively Growing Clouds With Vertical Updrafts

VISHNU NAIR*

Department of Civil and Environmental Engineering,Imperial College London, UK

THIJS HEUS

Department of Physics, Cleveland State University, USA

MAARTEN VAN REEUWIJK

Department of Civil and Environmental Engineering, Imperial College London, UK

ABSTRACT

The dynamics of a subsiding shell at the edges of actively growing shallow cumulus clouds with updrafts is analyzed using direct numerical simulation. The actively growing clouds have a fixed in-cloud buoyancy and velocity. Turbulent mixing and evaporative cooling at the cloud edges generate a subsiding shell which grows with time. A self-similar regime is observed for first and second order moments when normalized with respective maximum values. Internal scales derived from integral properties of the flow problem are identified. Self-similarity analysis conducted by normalizing using these scales reveal that contrary to classical self similar flows, the turbulent kinetic energy budget terms and velocity moments scale according to the buoyancy and not with the mean velocity. The shell thickness is observed to increase linearly with time. The buoyancy scale remains time-invariant and is set by the initial cloud-environment thermodynamics. The shell accelerates ballistically with a magnitude set by the saturation value of the buoyancy of the cloud-environment mixture. In this regime, the shell is buoyancy driven and independent of the in-cloud velocity. Relations are obtained for predicting the shell thickness and minimum velocities by linking the internal scales with external flow parameters. The values thus calculated are consistent with the thickness and velocities observed in typical shallow cumulus clouds. The entrainment coefficient is a function of the initial state of the cloud and the environment, and is shown to be of the same order of magnitude as fractional entrainment rates calculated for large scale models.

1. Introduction

Shallow cumulus convection is one of the most important unresolved processes in a global climate model. Parameterizations for vertical convective transport of momentum, heat and moisture include the effect of entrainment of environmental air into the cloud core, and the detrainment of the cloud core air into the environment (de Rooy et al. 2011). Most current operational climate models use parameterizations based on lateral mixing in a bulk approximation of entire fields of clouds. Numerous observational and model studies, especially using Large Eddy Simulations (LES) have shown that lateral mixing and entrainment is the dominant contributor towards cloud dilution (de Rooy et al. 2011; Taylor and Baker 1991; Heus et al. 2008). However, a precise picture of the mixing characteristics is still not available and studies on fundamental understanding and parameterization of entrainment in cumulus clouds remain an active field of current research (de Rooy et al. 2011).

The turbulent mixing at cloud edges results in the formation of a 'shell' of negatively buoyant layer of air around the cloud which adds to the complexity in studying and parameterizing entrainment in shallow cumulus clouds. The majority of mass-flux based parameterization schemes (Siebesma et al. 2003; Neggers et al. 2009; Tiedtke 1989), use a bulk parameterization to calculate the entrainment and detrainment rates into and from the cloud cores. In such approximations, the properties of the entrained and detrained air are considered to be that of the averaged properties of the environmental air and the cloud cores respectively. With the increase of resolution in weather models, cumulus convection has entered the grey zone, and has become partially resolved. At those resolutions, bulk parameterizations are no longer valid, and a more detailed understanding of mixing on a cloud-by-cloud is necessary (Neggers 2015). However, direct measurements of the entrainment and detrainment rates by Romps (2010)

*Corresponding author address: Department of Civil and Environmental Engineering, Imperial College London, South Kensington Campus, London, UK.
E-mail: vs2016@imperial.ac.uk

show values twice as high as the ones used in current parameterization schemes. This difference was attributed to the presence of these shells which makes it important to include the dynamics of the shell in parameterizations of cumulus clouds in GCMs (Dawe and Austin 2011; Park et al. 2016; Hannah 2017). Jonker et al. (2008) suggested that the majority of the upward mass flux in the cloud core is compensated by the downward mass flux in the shell, thus rendering cumulus clouds much less effective mixers than previously thought.

One of the early observations of the shell was done by Jonas (1990), who observed a thin descending layer of negatively buoyant air at the edges of developing and maturing shallow cumulus clouds. Rodts et al. (2003) used aircraft data from a large number of flight legs through cumuli and observed the shell of descending air. However a conspicuous dip in the profiles of the virtual potential temperature suggested that these shells were not formed as a result of mechanical forcing but by evaporative cooling due to entrainment and mixing with warm unsaturated environmental air. Heus and Jonker (2008) performed LES simulations and compared the simulation data with the observations of Rodts et al. (2003). They agreed with the conclusion that evaporative cooling was the driving force behind the subsiding shell by analyzing the individual terms in the vertical momentum budget. The findings of Wang et al. (2009) further corroborated these observational and LES results and provided evidence for evaporative cooling being the reason for the buoyancy driven shells.

The importance of the shells was further magnified by the analysis done by Jonker et al. (2008) and Heus et al. (2009) which resulted in the dual conclusion that upward transport in shallow clouds are concentrated more at the cloud boundaries rather than the cloud core, and downward transport is dominated in the area close to the boundaries as a result of the subsiding shells. The integral negative mass flux in this shell is significant and almost compensates the upward mass flux through the cloud core region.

There has been a general consensus that local processes at the cloud edge generate these shells. Most studies attribute the existence of the shell to evaporative cooling (Heus and Jonker 2008; Jonker et al. 2008). However, recent studies (Park et al. 2016, 2017) suggest that buoyancy reversal at the cloud edge occurs even in a modified LES where evaporative cooling is absent. Park et al. (2016) speculates that the downdrafts in the boundary layer are generated by overturning vortex-like circulations similar to Hill's vortex (Hill 1894) as proposed by Sherwood et al. (2013), which are then strengthened by evaporative cooling in the cloud layer; while Park et al. (2017) propose that they are generated instead by convective mixing across vertical levels and condensation in the cloud.

The dynamic properties of these shells have been previously studied using observational data and numerical simulations- mainly LES. LES studies are unable to resolve the finer details of cloud-edge mixing. Given that the typical width of the shell is usually close to the resolution of the LES, Direct Numerical Simulation (DNS) studies are much more effective when it comes to capturing small-scale dynamics as they resolve scales down to the Kolmogorov scale. But DNS studies have been few, and always with simple idealized models.

The first DNS at the cloud edge was performed by Abma et al. (2013) to explore the characteristics of the shell and to obtain scaling laws for its evolution under buoyancy reversing conditions. Since DNS resolves the entire turbulent spectrum, it is expensive and beyond current computational capabilities to resolve an entire cloud. Hence only the flow immediately around the cloud edge is considered. A highly idealized setup was used which ignores important properties such as in-cloud buoyancy, vertical velocity, turbulence and cloud microphysics. This idealization, as fairly mentioned in the work is "likely to create an overestimation of the strength of the subsiding shell". Perrin and Jonker (2015) also used a mixing layer to study cloud edges but with DNS combined with a Lagrangian particle tracking and collision algorithm. This study was more focused on studying the effect of evaporation, gravity, coalescence, and the initial droplet size distribution on the intensity of the mixing layer and the evolution of the droplet size distribution. However both simulations were highly transient to study the dynamic properties of the shell. The results of the DNS performed by Abma et al. (2013) were compared with observations by Katzwinkel et al. (2014) who performed measurements of the structure of cloud edges for trade wind cumuli. They studied turbulent, thermodynamic and microphysical structures. Since the measurements were taken over the trade wind region where there is a continuous development of the shallow cumulus clouds during the day, the shell properties were studied as the cloud evolves through different stages. They observed that the shell thickness varied according to the evolution stage of the cloud. This provides additional motivation to develop a setup which could simulate an actively growing cloud.

The goal of this work is to study the cloud-clear interface while taking the presence of the in-cloud updraft into account. The set-up is to be designed as close to actual actively growing cloud conditions; with a distinct cloud core with updrafts, surrounded by a thin subsiding shell layer with downdrafts. We study how the shell evolves dynamically under the effects of evaporative cooling and turbulent mixing, investigate if the flow reaches a self-similar regime thus establishing Reynolds number independence, and obtain scaling laws for the growth of the shell. We also develop a simplified model to quantify the turbulent entrainment in the cloud.

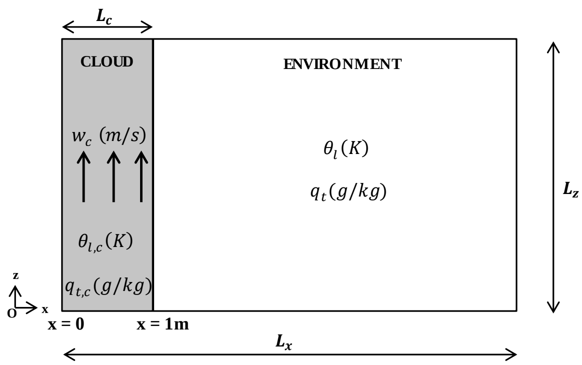

FIG. 1. Two-layer cloud-environment simulation setup

This paper is structured as follows. In section 2 we explain the case setup, governing equations and the details of the simulations performed. In section 3 we present initial results that identifies the subsiding shell. In section 4, the self-similarity aspects of the flow is investigated. In section 5 the characteristic scales for the flow are identified. Section 6 includes a theoretical analysis to identify the processes which govern the flow in the shell. In section 7 the results from all the simulations are shown to study how the shell properties are influenced by the initial thermodynamics of the cloud and environment. Section 8 includes a discussion of the results from the simulations and concluding remarks.

2. Simulations

a. Case setup

The simulations are temporal flow experiments in which the development of a small region at the edge of a shallow cumulus, including both the cloud and the surrounding environment, is studied. Specifically, we consider a two layer cloud-environment set-up, in which the domain is divided into a moist, positively buoyant cloud layer and a dry, neutrally buoyant environment layer, with the gravity vector aligned in the vertical direction $\hat{z}$ as shown in figure 1. The cloud has a positive buoyancy b_c and an in-cloud velocity w_c and hence resembles an actively growing cloud as defined in Katzwinkel et al. (2014). The liquid water potential temperature θ_l, and the total water specific humidity q_t, define the thermodynamic properties of the cloud and the environment. As in Abma et al. (2013), the dominant mixing is assumed to occur locally and hence the influence of the cloud top and base can be neglected which makes the system statistically homogeneous in the vertical direction $\hat{z}$. This allows us to impose periodic boundary conditions on the top and bottom boundaries and in the span-wise direction if the domain is large enough. Hence statistics can be obtained by averaging over the yz-plane.

In test simulations, it was observed that the negatively buoyant layer formed at the cloud edge grows at the expense of the cloud. The cloud-environmental air mixture soon exhausts the entire cloud layer and descends as a single fluid mass. As mentioned in the introduction, this is a very transient process and does not provide an ideal setup to study the dynamic properties of the shell. In order to overcome this problem and study the properties of the subsiding shell in an actively growing cloud, a volumetric forcing is applied to the cloud layer which nudges the vertical velocity and thermodynamic properties of the cloud towards pre-defined values. This is a way to constantly 'replenish' the cloud layer and hence mimic the conditions in an actively growing cloud.

The governing equations are

$$\nabla \cdot \mathbf{u} = 0, \tag{1a}$$

$$\frac{\partial \mathbf{u}}{\partial t} + \mathbf{u}\cdot\nabla\mathbf{u} = -\nabla p + \nu\nabla^2\mathbf{u} + b\,\mathbf{e}_z + \frac{w_c - w}{\tau}\,\mathbf{e}_z\,H(L_c - x), \tag{1b}$$

$$\frac{\partial \chi}{\partial t} + \mathbf{u}\cdot\nabla\chi = K\nabla^2\chi + \frac{\chi_c - \chi}{\tau}\,H(L_c - x). \tag{1c}$$

where, $\mathbf{u} = (u, v, w)$, is the velocity vector with u, v and w as the horizontal, transverse and vertical components respectively. The variable χ represents the scalars (θ_l, q_t), p is the kinematic pressure, ν is the kinematic viscosity, K represents the diffusivity constants (κ, D) where κ is the thermal diffusivity of air and D is the molecular diffusivity of water. Parameters w_c and χ_c are the nudging values maintained in the cloud layer, H is the Heaviside function, L_c is the width of the initial cloud layer, $\mathbf{e}_z$ is the unit vector along the vertical direction and τ is a nudging time scale for the forcing.

The buoyancy b is given by

$$b = g\left(\frac{\theta - \theta_0}{\theta_0} + \frac{R_d}{R_v}(q_t - q_{t,0}) - \frac{R_v}{R_d}q_l\right), \tag{2}$$

where θ is the potential temperature, q_l is the liquid water specific humidity, θ_0 and $q_{t,0}$ are the corresponding environmental values, $R_d = 287.0$J/kg/K and $R_v = 461.5$ J/kg/K are the gas constants for dry air and water vapour respectively. A bulk condensation scheme developed by Sommeria and Deardorff (1976) is used to diagnostically calculate q_l.

The DNS code SPARKLE is used, which solves the incompressible Navier-Stokes equations under the Boussinesq approximation, and transport equations for scalars to fourth order accuracy. Details of the numerical method used in SPARKLE and other details can be found in Craske and van Reeuwijk (2015).

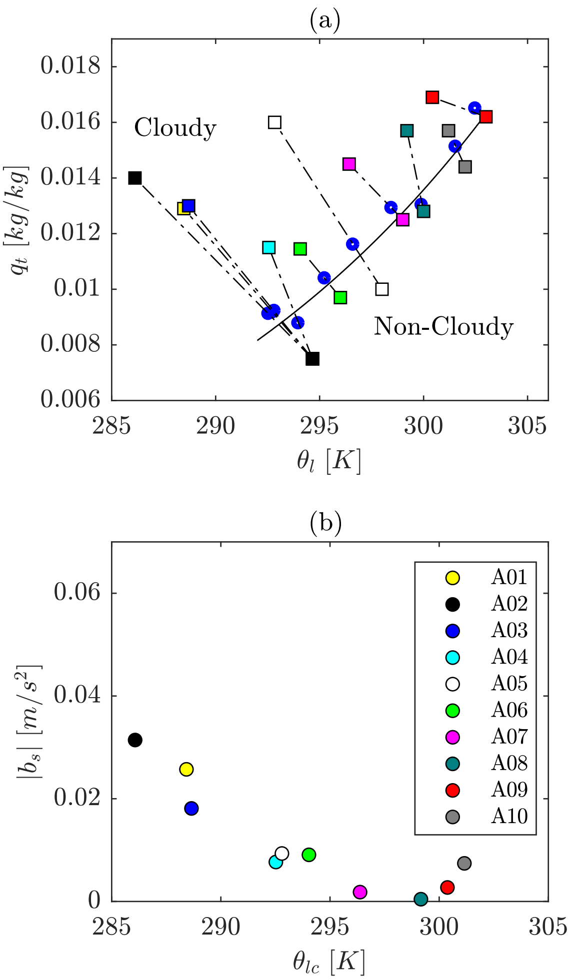

FIG. 2. (a) Temperature-humidity diagram representing different initial states for cloud and environment. Black line represents the saturation curve, squares represent the properties of the initial states of the cloud and environment layer, and the dot-dash line represents the mixing line. The property of the mixed parcels with minimum mean buoyancy is represented by circles. (b) Magnitude of buoyancy minima in the shell b_s against θ_{lc}, the initial value of θ_l in the cloud for different simulations.

b. Simulation details

A temperature-humidity diagram relating q_t and θ_l is shown in figure 2. The continuous line represents the saturation curve. The initial values of the thermodynamic properties θ_l and q_t are represented by squares, where all the squares above the saturation curve represent the cloud and those below represent the environment. The range of initial cloud and environment properties vary from $\theta_l \approx 286K \rightarrow 303K$ and $q_t \approx 7.5g/kg \rightarrow 17g/kg$. Assuming linear mixing, the thermodynamic states of the cloud-environmental air mixture can be approximated to lie along a mixing line (dot-dash) between these two squares. The mean properties of the saturated mixtures for each of the simulations can then be considered to be lying on the saturation curve. The point where this mixing line crosses the saturation curve gives the properties of the critically saturated mixture, $\theta_{l,s}$ and $q_{t,s}$. These values can be used to determine the magnitude of the buoyancy minima in the shell b_s (shown in bottom panel of figure 2). The circles denote the point $(\theta_{l,s}, q_{t,s})$ obtained from the DNS for each of the simulations and they lie very close to the saturation curve hence showing that this approximation works well.

The cloud layer extends up to L_c in the cross-stream direction and the forcing is applied in this region. The initial buoyancy and vertical velocity distributions are homogeneous in the $\hat{z}$ and $\hat{y}$ directions. Periodic boundary conditions are imposed along these directions as well. Free-slip boundary conditions are imposed along the $\hat{x}$ direction. This setup results in the mean values having non-zero gradients only along the $\hat{x}$ direction. The forcing is applied across the cloud layer till $L_c = 1m$ over a time scale given by $\tau = L_c/w_c$. To ensure that results were not influenced by these arbitrary parameters, a sensitivity analysis was performed in which two test simulations were performed: the first by relaxing the nudging time scale to 2 L_c/w_c, and a second simulation by doubling L_c to $2m$. The results obtained indicate that the flow dynamics are insensitive to the choice of L_c and τ (shown in appendix).

The domain size is $30m$ x $15m$ x $15m$. The simulations are performed until the shell reaches about 70 percent of the domain width (in $\hat{x}$ direction) so as to avoid any effects from interference with the domain wall boundary.

The simulations named A01 - A10 vary in the initial θ_l and q_t of the cloud and environment, and the strength of the cloud updraft w_c as shown in table 1. The difference in the initial values of the scalars $\Delta\theta_l$ and Δq_t across the cloud-environment interface are shown in the third and fourth columns. The initial values of θ_l and q_l in the cloud layer are given by θ_{lc} and q_{lc} respectively. The simulations are run for a duration given by t_{sim}. The remaining parameters shown in the table (to the right of the double-vertical line) are obtained from the simulation: the magnitude of the minimum mean buoyancy in the shell b_s, the Taylor Reynolds number $Re_\lambda = \sqrt{\frac{2k\lambda/3}{\nu}}$,where $\lambda = \sqrt{\frac{10\nu k}{\varepsilon}}$ is the Taylor micro-scale, ν is the fluid kinematic viscosity, k and ε are the integral turbulent kinetic energy and dissipation respectively within the shell, and the resolution $r = \Delta x/\eta$ where η is the Kolmogorov length scale. The domain is discretized into a uniform grid of 3072 x 1536 x 1536 points for simulations A01, A04 and A09, and a grid of 1536 x 768 x 768 for all other simulations. The simulations were performed on the UK supercomputer ARCHER with A01 running on 683 nodes (using 16,384 cores) for 20 hours (CPU time).

TABLE 1. Simulation parameters. Parameters to the left of the double vertical line are from the initial setup and those to the right are diagnosed from the simulation results.

Sim No	Grid size	$\Delta\theta_l(K)$	$\Delta q_t(g/kg)$	$\theta_{lc}(K)$	$q_{lc}(g/kg)$	$w_c(m/s)$	$t_{\text{sim}}(s)$	$b_s(m/s^2)$	Re_λ	$\Delta x/\eta$
A01	3072 x 1536 x 1536	-6.2	5.4	288.5	3.0	0.81	148	-0.022	95.1	0.62
A02	1536 x 768 x 768	-8.1	6.3	286.1	4.3	0.96	120	-0.025	70.3	0.89
A03	1536 x 768 x 768	-5.9	5.5	288.7	3.0	0.81	120	-0.018	61.1	0.78
A04	3072 x 1536 x 1536	-2.1	4.0	292.6	1.3	0.67	148	-0.0073	90.3	0.33
A05	1536 x 768 x 768	-5.2	6.0	292.8	3.0	0.52	148	-0.0088	102.7	1.39
A06	1536 x 768 x 768	-1.9	1.8	294.1	0.8	0.31	180	-0.0088	36.5	0.76
A07	1536 x 768 x 768	-2.6	2.0	296.4	1.3	0.31	240	-0.0014	60.9	0.62
A08	1536 x 768 x 768	-0.8	2.9	299.2	0.9	2.03	100	-0.0002	47.8	0.52
A09	3072 x 1536 x 1536	-2.6	2.0	300.4	1.2	0.43	220	-0.002	53.8	0.30
A10	1536 x 768 x 768	-0.8	1.3	301.2	0.3	2.00	120	-0.007	64.7	0.82

3. Shell identification

Simulation A01 is taken as the base simulation. The turbulent mixing between the cool and moist cloudy air and the warm, dry environmental air, leads to evaporation (initially present only in cloudy area) until the mixture becomes critically saturated. The evaporative cooling at the mixing zone in the cloud edge results in the layer becoming negatively buoyant as the temperature scalar is no longer passive, and is coupled to the flow buoyancy. We refer to the negatively buoyant layer as the 'shell', and to the negatively buoyant layer with negative vertical velocity as the 'subsiding shell'.

Figure 3 shows the development of the subsiding shell at the cloud boundary. The snapshots show the instantaneous buoyancy b, and vertical velocity w at different time intervals for simulation A01. The white filaments correspond to zero magnitude, and red and blue layers represent positive and negative regions respectively. As found in Abma et al. (2013), buoyancy drives the flow and the sharp interface between the cloud and the environment evolves to convoluted filaments. The layer at the edge of the cloud becomes negatively buoyant early on in the simulation, and the thickness of the shell increases with time. However even when b is negative, at earlier times, the velocity still remains positive or close to zero. As the shell thickens, we start seeing the formation of the subsiding shell.

Figure 4 shows profiles of the mean buoyancy $\overline{b}$ and the mean vertical velocity $\overline{w}$ of the developing flow at the cloud boundary. As mentioned in the introduction, the flow can be considered homogeneous over the vertical direction $\hat{z}$ and the span-wise direction $\hat{y}$. Hence all the quantities are averaged over the yz plane. Additionally the quantities are averaged over a time interval of $4s$. Hence the over-bar denotes statistics averaged over the homogeneous yz-plane and a time interval $t_{stat} = 4s$. For example, the mean buoyancy $\overline{b}(x,t)$ is calculated as,

$$\overline{b}(x,t) = \frac{1}{t_{stat}} \int_0^{t_{stat}} \left[\frac{1}{L_y L_z} \iint_{\hat{y}\hat{z}} b(x,y,z,t)\, dy\, dz \right] dt \qquad (3)$$

Results are shown every $8s$ from $t = 48s$ to $t = 112s$ for simulation A01. We observe the formation of the negatively buoyant shell and its thickening with time. The magnitude of the minima for $\overline{b}$ and $\overline{w}$, $\overline{b}_{\min}(t)$ and $\overline{w}_{\min}(t)$ respectively, are also shown along with their respective locations along $\hat{x}$, x_b^0 and x_w^0. The bounds of the negatively buoyant layer ($x_b^{\pm}$), and negative vertical velocity ($x_w^{\pm}$) are also shown. These are respectively, the locations along $\hat{x}$ where the quantities first turn negative (x_b^-, x_w^-) and then positive again (x_b^+, x_w^+).

Figure 4 clearly shows the shell growing and thickening with time. From figure 4(a), it is clear that after an initial transient period, the minimum buoyancy $\overline{b}_{\min}(t)$ is time-invariant. This occurs when the cloud-air mixture is critically saturated as will be explained rigorously in section 5. Figure 4 also shows how x_b^- and x_b^+ shifts as the shell broadens with time. The inner boundary of the shell x_b^-, is observed to shift only by a very small distance, which allows us to consider it constant. The outer boundary of the shell is observed to shift outwards into the environment. Contrary to the mean buoyancy, the minimum magnitude of the velocity is not time-invariant and figure 4(b) clearly shows the shell accelerating downwards. Figure 4 hence gives a clear picture of a negatively buoyant mixture of cloudy and non-cloudy air accelerating downwards, i.e. a subsiding shell. In both figures we observe a lateral shift in the locations of the minima, x_b^0 and x_w^0. The location of the minima moves outwards into the environment as the shell thickens.

In figure 5, the area in the numerical domain where $\overline{b}$ and $\overline{w}$ is negative is shown in red and blue respectively. The flow studied over 148 s can be considered to include two phases, each consisting of negatively buoyant parcels

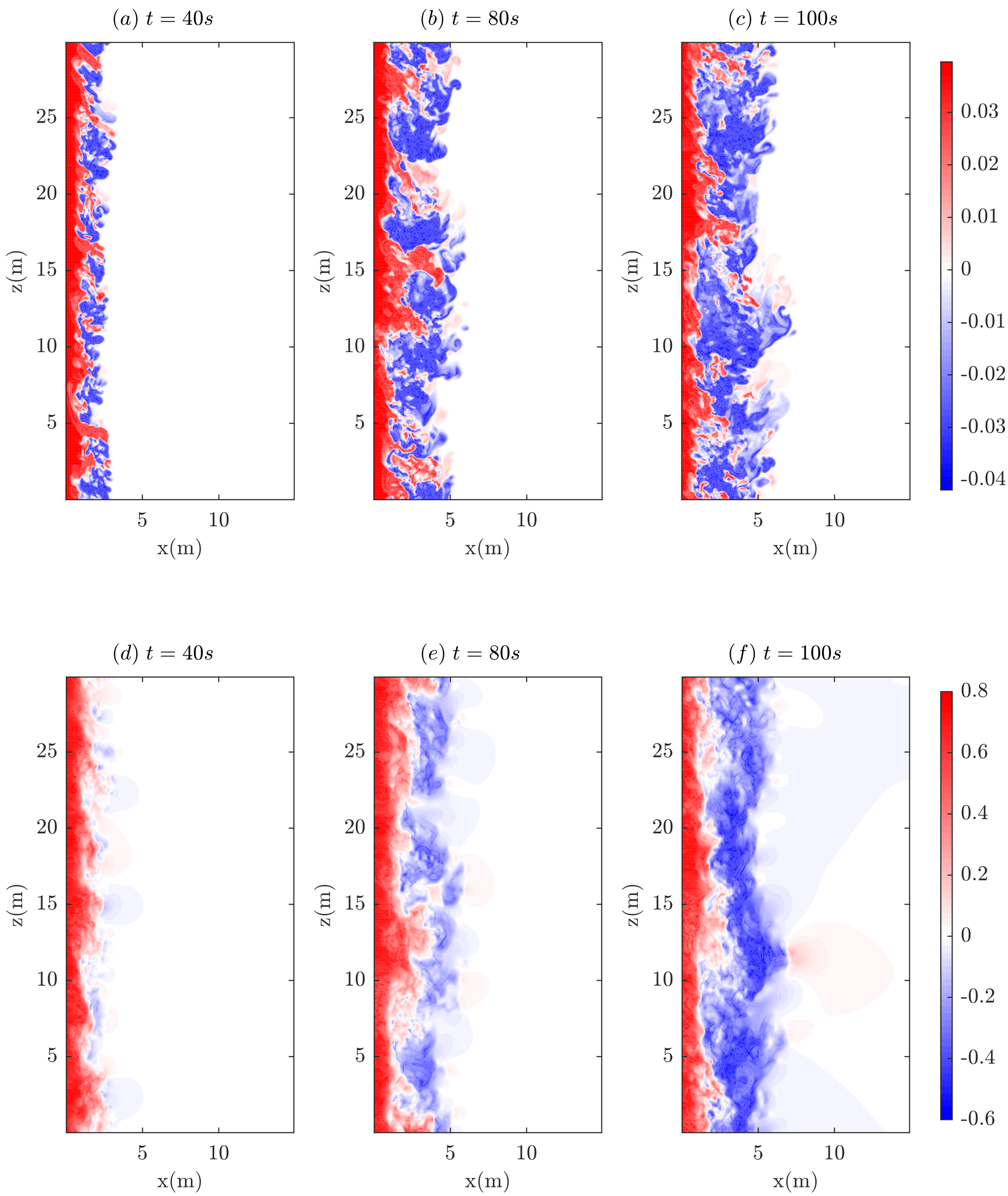

FIG. 3. Instantaneous plots of the vertical cross-section of the flow. Top panel shows the evolution of buoyancy and bottom panel shows the evolution of vertical velocity. Red represents positive values and blue negative values with white representing zero.

of air, but with either positive or negative velocities. The first 'drag phase', i.e. when the cold layer is dragged up along the updraft, occurs during approximately the first 40s (which includes a flow transition period). In this phase, a negatively buoyant region is formed, but the mixed air parcels have positive vertical velocity. The second 'buoy-

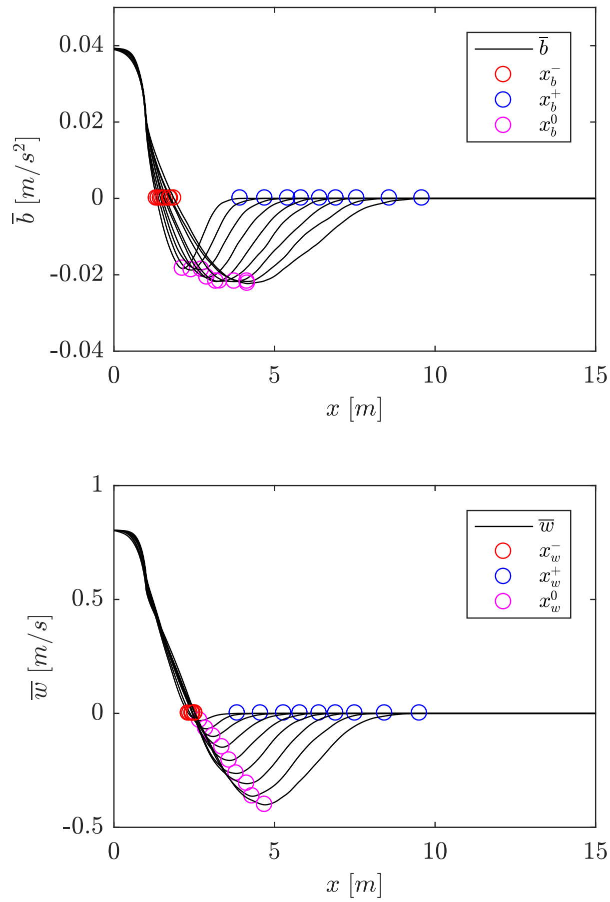

FIG. 4. Time series of (a) mean buoyancy $\overline{b}$, and (b) mean vertical velocity $\overline{w}$. Also shown are the locations x_b^-, x_b^+, x_w^-, x_w^+ where the quantities first turn negative and consequently turn zero again, and the location of the minimum magnitudes x_b^0 and x_w^0. Both plots show profiles every 8s from time 48s to 112s.

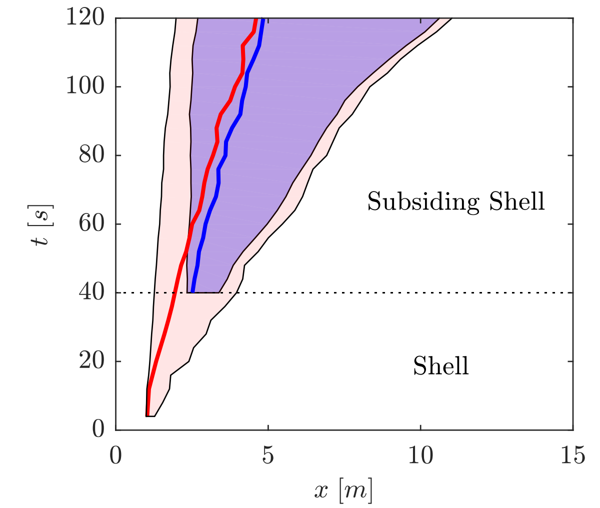

FIG. 5. Boundaries of the subsiding shell. The negatively buoyant mixture is shown in red and region with negative vertical velocity is in blue. The inner and outer bounds of the red region is x_b^- and x_b^+. Red line is x_b^0 and blue line is x_w^0.

ancy phase' starts once this cold layer starts moving downwards, i.e. the buoyancy dominates. The transition from the drag phase to the buoyancy phase occurs when the shear across the shell inner boundary dominates the buoyancy in the shell, and this is analysed in detail in section 6.

4. Self-similarity of the shell

In this section, we explore the self-similarity aspects of the flow. The self-similarity variable is defined as

$$\eta_b = \frac{x - x_b^0}{l_s}, \tag{4}$$

where $l_s(t) = x_b^+(t) - x_b^-(t)$ is the thickness of the shell calculated from DNS data.

The $\overline{b}$ profiles from time 96s to 140s neatly collapse on top of each other when normalized with $\overline{b}_{\min}$ as shown in figure 6a. The colours indicate progress in time (from lighter to darker). Also, given that the flow does not reach an 'equilibrium' state in the sense that the shell is accelerating, $\overline{w}$ shows a very good collapse when normalized with $\overline{w}_{\min}$ (figure 6b). The noticeable shift in most of the figures for η_b values less than -0.25 corresponds to the cloud layer in the domain where the nudging is applied.

Self similarity in the the mean turbulent kinetic energy (TKE) $\overline{k}$, and the turbulence fluxes $\overline{u'w'}$, $\overline{u'\theta_l'}$, and $\overline{u'q_t'}$ is investigated. The TKE is calculated as $\overline{k} = \frac{1}{2}(\overline{u'^2} + \overline{v'^2} + \overline{w'^2})$ where $\overline{u'^2}$, $\overline{v'^2}$ and $\overline{w'^2}$, are the measures of the turbulent fluctuations along x, y and z directions respectively. These quantities are normalized with their respective maxima. The results are shown in figures 6c, d, e and f where a satisfactory collapse is observed for the quantities which indicates self-similarity. All plots show profiles every 4s from 96s to 140s.

5. Characteristic scales

The previous section demonstrated a convincing self-similarity of the first and second order statistics. In this section, the different possible characteristic scales for this problem are explored. This can be done in several ways; one approach would be to relate the scales used to non-dimensionalize the profiles directly to external flow parameters and to time, as is done for example in van Reeuwijk et al. (2018). Another approach is to use internal scales, which are derived from integral properties of the flow problem (Craske and van Reeuwijk 2015). It is the latter approach that we will pursue initially. Once the relevant internal scales are identified, we link the internal scales to

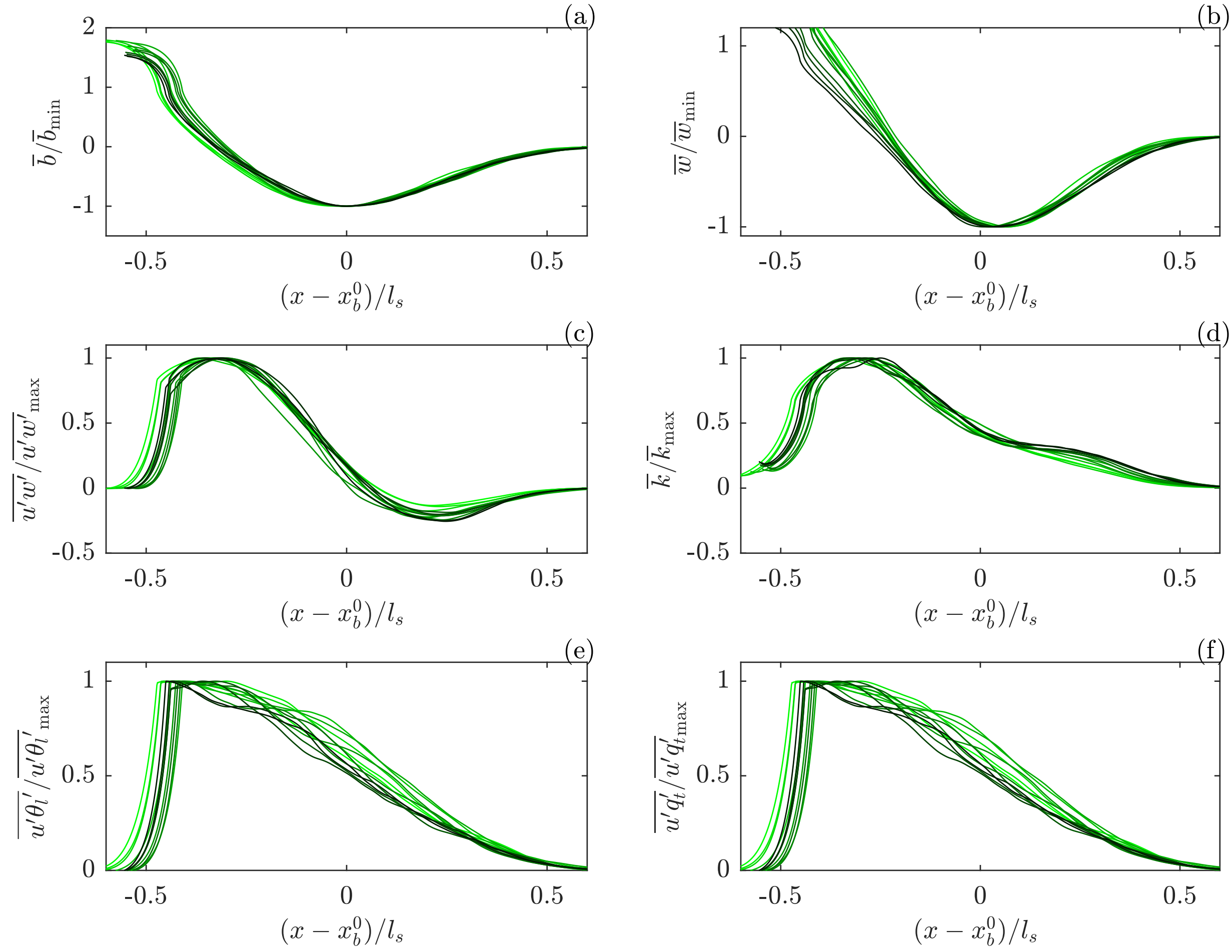

FIG. 6. Self similarity plots for shell. (a) $\overline{b}$ (b) $\overline{w}$, (c) $\overline{u'w'}$, (d) $\overline{k}$, (e) $\overline{u'\theta_l'}$, (f) $\overline{u'q_t'}$. All profiles are from time 96s to 140s. The colours indicate progress in time (from lighter to darker).

external scales; it will turn out that this problem does not quite behave like a classical self-similar flow.

We define characteristic scales using integral properties of the flow, namely the buoyancy integral B and the volume flux Q defined as,

$$B(t) = -\int_{x_b^-(t)}^{x_b^+(t)} \overline{b}(x,t)dx,$$

$$Q(t) = \int_{x_b^-(t)}^{x_b^+(t)} \overline{w}(x,t)dx.$$

The buoyancy integral B can be linked to the characteristic scales b^* and l^* as

$$B = b^* l^*. \tag{5}$$

The buoyancy of the mixture of cloudy and non-cloudy air, which were initially at two different thermodynamic states, reaches a minimum value when the mixture is critically saturated. Intuitively, the characteristic buoyancy scale b^* for this particular problem will be the saturation buoyancy b_s, i.e.

$$b^* = |b_s|. \tag{6}$$

The magnitude of b_s can be predicted *a priori* by using the mean values of the thermodynamic variables, i.e., $\overline{\theta}_l$ and $\overline{q}_t$. As explained in section 2, $\overline{q}_l = 0$ on the saturation curve shown in figure 2. From the definition for $\overline{\theta}_l$, it then follows that $\overline{\theta}_{l,s} = \overline{\theta}_s$ implying that b_s can be determined from equations 1c and 2 as

$$b_s = g\left(\frac{\overline{\theta}_s - \theta_0}{\theta_0} + \frac{R_d}{R_v}(\overline{q}_{t,s} - q_{t,0})\right). \tag{7}$$

The comparison between $|b_s|$ and $|\overline{b}_{\min}|$ gives very good agreement as shown in figure 7a. The saturation point is set by the initial thermodynamics of the cloud and the environment and we observe it to be invariant with time as we assume linear mixing.

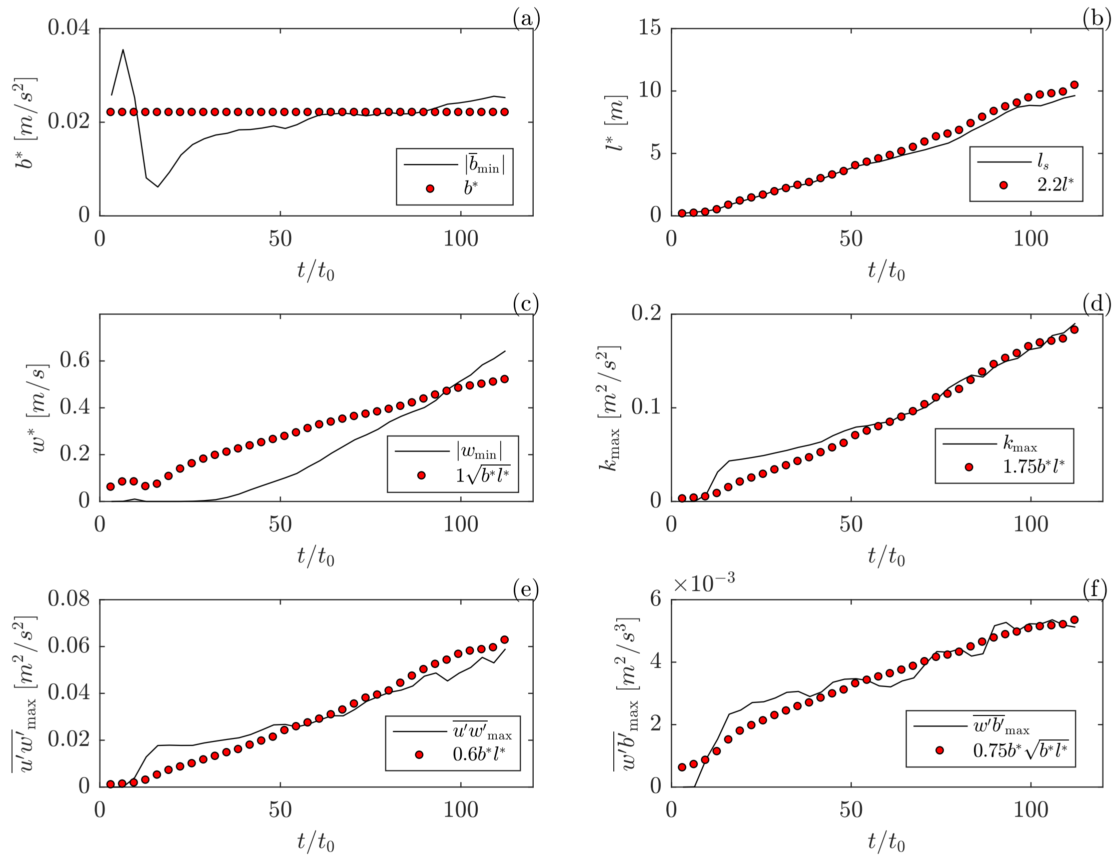

FIG. 7. Relationship between (a) buoyancy scale b^* and $|b_{min}|$, (b) length scale l^* and l_s, (c) velocity scale w^* and $|w_{min}|$, (d) maximum total kinetic energy $k_{\max}$ and b^*l^*, (e) maximum turbulent momentum flux $\overline{u'w'}_{\max}$ and b^*l^*, and (f) maximum turbulent buoyancy production $\overline{w'b'}_{\max}$ and $b^*\sqrt{b^*l^*}$. The x-axis is normalized with $t_0 = L_c/w_c$.

Once the buoyancy scale b^* has been defined, the characteristic shell width l^* follows directly as

$$l^* = \frac{B}{b^*}, \tag{8}$$

which can be interpreted as the top-hat width of the shell (i.e. the width in case the buoyancy was constant inside the shell). Figure 7(b) shows that this definition is indeed appropriate, and we observe a relation $l_s = 2.2l^*$. The x axis has been normalized with $t_0 = L_c/w_c$. The length scale l^*, which is a measure of the shell thickness, is also observed to evolve linearly with time in figure 7b. Abma et al. (2013) observed a quadratic growth in their idealized model. However, the current study includes factors which limit the free growth of the shell, such as the in-cloud positive buoyancy and the velocity, which could be the reason for the linear growth of the shell thickness.

A characteristic velocity scale is identified next. Since b^* and l^* are characteristic scales for this problem, it would follow that the characteristic velocity scales as $\sqrt{b^*l^*}$. This velocity scale is tested in figure 7c. It is clear that the velocity scale $\sqrt{b^*l^*}$ is not representative of the shell velocity. However, remarkably, the turbulence kinetic energy k and turbulent horizontal transport of vertical momentum $\overline{u'w'}$ *do* scale with $\sqrt{b^*l^*}$ as shown in figures 7d and e, and the buoyancy TKE production term $\overline{w'b'}$ scales with $b^*\sqrt{b^*l^*}$. The shell is also observed to be accelerating as is shown in the linear growth of the velocity scale w^* in figure 7c. A 'flow equilibrium' or a steady state is not reached, and the velocity shows a possible ballistic growth with time with an acceleration defined by b^* and hence the thermodynamics of the cloud.

The collapse of the different terms of the TKE budget are now tested to confirm the ballistic growth of the shell argument. The budget quantities are normalized with the internal characteristic scales b^* and l^*. The different components of the averaged TKE budget, i.e., the kinetic energy production terms (gradient and buoyancy production), transport terms and the viscous dissipation are examined. The TKE budget is given by

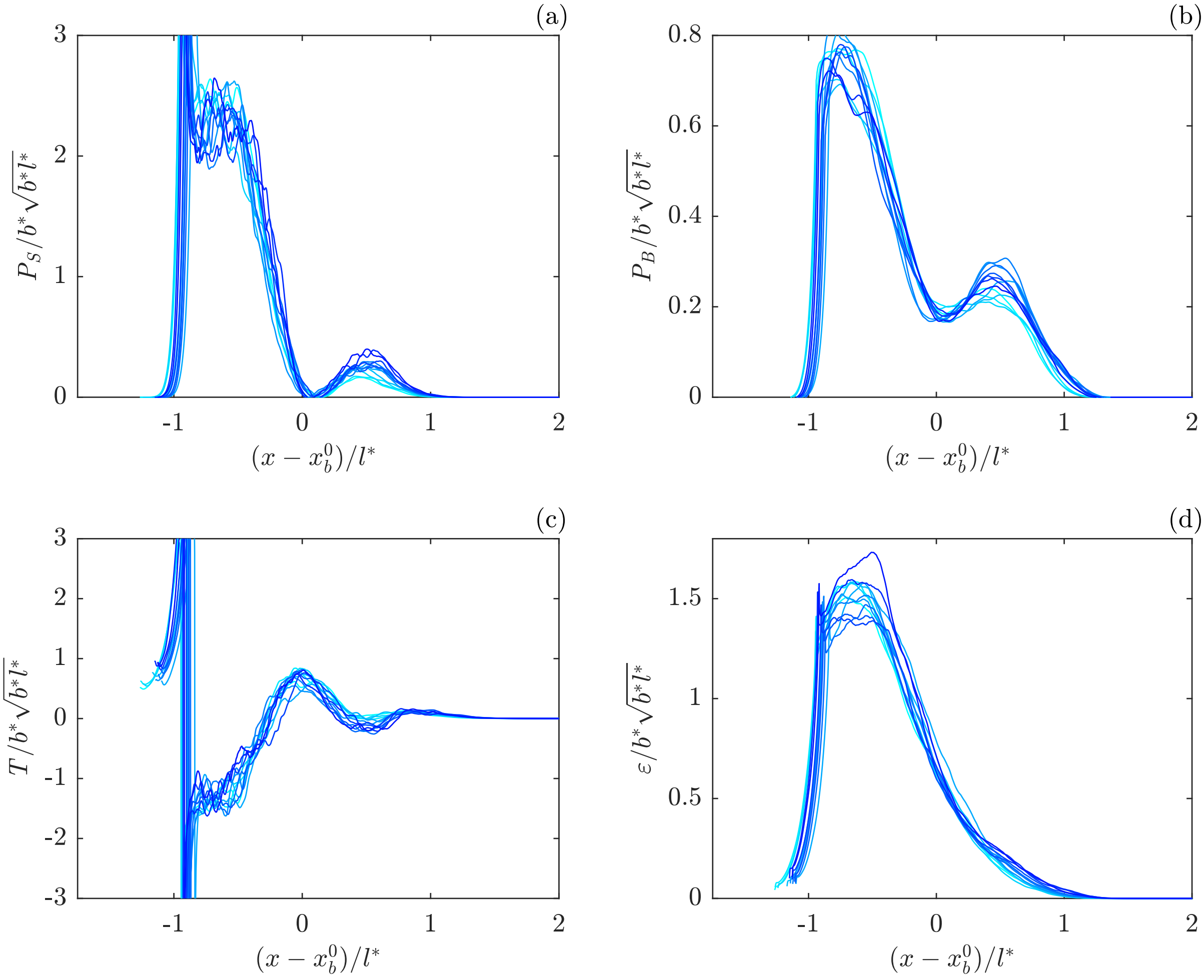

FIG. 8. Scalings for TKE budget quantities. (a) P_S, the shear production, (b) P_B, the buoyancy production, (c)T, the transport term and (d) ε, the viscous dissipation rate of TKE. All profiles are from time $96s$ to $140s$. The colours indicate progress in time (from lighter to darker).

$$\frac{\partial k}{\partial t} = \underbrace{-\overline{u'w'}\frac{\partial \overline{w}}{\partial x} + \overline{w'b'}}_{P_S+P_B} \quad (9)$$
$$\underbrace{-\frac{\partial \overline{u'p'}}{\partial x} - \frac{\partial \overline{u'u_i'u_i'}}{\partial x} + \nu\frac{\partial^2 k}{\partial x^2}}_{T} \underbrace{- \nu\overline{\frac{\partial u_i'}{\partial x_j}\frac{\partial u_i'}{\partial x_j}}}_{\varepsilon},$$

where $k = \frac{1}{2}\overline{u_i'u_i'}$ and repeated indices in a term imply a summation for all values of the repeated index. The term P_S denotes shear production and P_B is the buoyancy production term or the buoyancy flux. The next three terms combine to form the transport term T which includes the pressure transport term, turbulent advective transport and the diffusive transport of kinetic energy. The last term ε is the viscous dissipation rate of TKE.

Good collapse of the turbulent quantities are shown in figure 8(a) - (d) when scaled with the buoyancy scale b^* and length scale l^* which are calculated according to equations 6 and 8. The mean flow velocity is not important in generating and driving the shell and this renders the velocity scale w^* passive. The mean velocity is slaved to the buoyancy effects and hence the turbulent quantities scale with the buoyancy scale b^*.

6. Theory

In this section, we carry out a theoretical analysis to identify the processes which generate the different phases observed in the flow. We also identify how the shell is fed with the buoyancy which drives the flow.

We start with Reynolds averaged (over the two homogeneous axes) equations for the vertical velocity and bu-

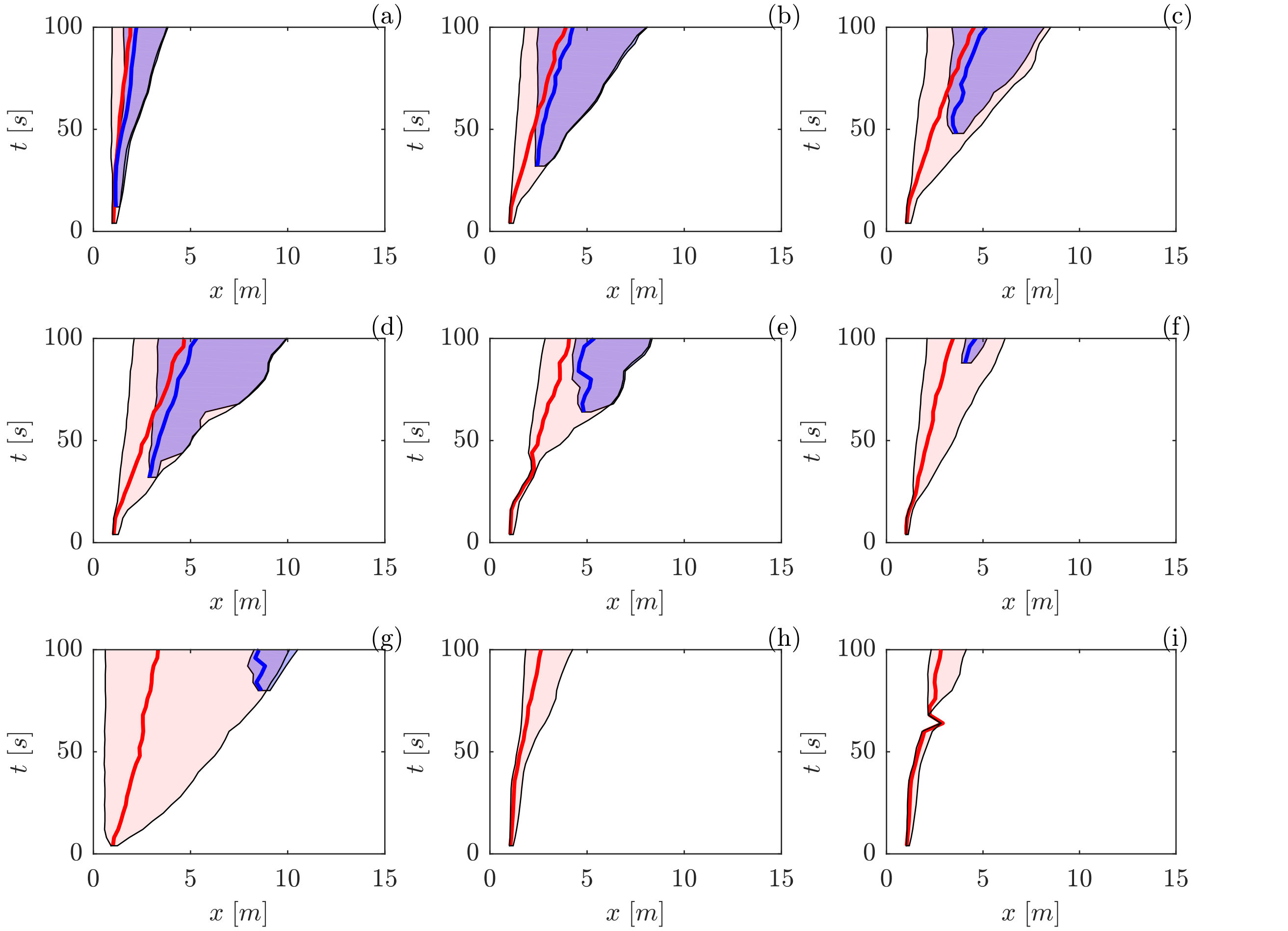

FIG. 9. Cloud-environment mixing region for different simulations. (a) A06,(b) A01 (c) A03, (d) A02, (e) A05 (f) A04 (g) A10 (h) A09 (i) A07. Line styles and color schemes are identical to figure 5.

oyancy using equations 1b and 1c,

$$\frac{\partial \overline{w}}{\partial t} + \frac{\partial \overline{u'w'}}{\partial x} = \overline{b} + S_1, \tag{10}$$

$$\frac{\partial \overline{b}}{\partial t} + \frac{\partial \overline{u'b'}}{\partial x} + g\left(\frac{A}{\theta_0} - \frac{R_v}{R_d}\right)\left(\frac{\partial \overline{q}_s}{\partial t} + \frac{\partial \overline{u'q_s'}}{\partial x}\right) = g\left[\frac{S_2}{\theta_0} + \left(\frac{A}{\theta_0} - 1\right)S_3\right], \tag{11}$$

where $A = \frac{\theta}{T}\frac{L_v}{c_p}$ is assumed to be a constant, and S_1, S_2, S_3 are the Reynolds averaged terms for the cloud forcing. Integrating equation 10 from the shell inner boundary $x_b^-(t)$ to the shell outer boundary $x_b^+(t)$ results in,

$$\frac{dQ}{dt} = B + \left(\overline{w}|_{x_b^-}\frac{dx_b^-}{dt} - \overline{w}|_{x_b^+}\frac{dx_b^+}{dt}\right) + \overline{u'w'}|_{x_b^-} - \overline{u'w'}|_{x_b^+}. \tag{12}$$

The budget equation for the volume flux Q is vital towards explaining the presence of the drag and buoyancy flow phases in the shell. The terms at the shell outer boundary x_b^+, along with the Leibnitz integral term at x_b^-, are observed to be small and hence neglected. The remaining terms highlight the fact that the flow inside the shell is determined by a balance between B, the buoyancy integral, and $\overline{u'w'}|_{x_b^-}$, the horizontal transport of vertical momentum at the inner boundary of the shell. The onset of the buoyancy phase happens when the negative integral buoyancy flux B in the shell overcomes the vertical momentum flux $\overline{u'w'}$ transferred horizontally into the shell at x_b^-, which results in a reversal in the direction of the shell velocity. When $\overline{u'w'}|_{x_b^-}$ dominates the budget, we have the drag phase identified in section 3, i.e., the cold layer is dragged up by the cloud updraft. As B increases with time and consequently overcomes the momentum flux, the negatively buoyant layer reverses its direction and we start seeing the subsiding shell.

Equation 11 is now integrated from $x_b^-(t)$ to $x_b^+(t)$ giving,

$$\frac{\mathrm{d}B}{\mathrm{d}t} = \overline{u'b'}|_{x_b^-} - \overline{u'b'}|_{x_b^+} + g\left(\frac{A}{\theta_0} - \frac{R_v}{R_d}\right)\int_{x_b^-}^{x_b^+}\left(\frac{\partial \overline{q}_s}{\partial t} + \frac{\partial \overline{u'q_s'}}{\partial x}\right)\mathrm{dx}, \tag{13}$$

Analyzing the different terms in equation 13, the third term on the right hand side can be shown to be equal to zero in the region $x > L_c$. It is also observed that the magnitude of $\overline{u'b'}|_{x_b^-}$ (not shown) is time-invariant for a particular simulation, and that of $\overline{u'b'}|_{x_b^+}$ is negligible. Hence the dominant term in the B budget is $\overline{u'b'}|_{x_b^-}$, which is the buoyancy flux at the inner boundary of the shell. Assuming $\overline{u'b'}|_{x_b^-} \approx$ constant, and neglecting all small terms, $B = \int \overline{u'b'}|_{x_b^-} dt$. This shows that the total amount of buoyancy flux $\overline{u'b'}$ fed into the shell by the cloud ultimately drives the turbulent flow and is responsible for feeding the shell buoyancy and hence increasing its thickness.

Since the magnitude of $\overline{u'b'}|_{x_b^-}$ is observed to be time-invariant, a possible parameterization using w_c and b_c follows as

$$\overline{u'b'}|_{x_b^-} = \gamma w_c b_c, \tag{14}$$

where γ is a constant whose values for the different simulations are given in table 2. This parameterization is used in the following section to explain the possible external factors that define the shell thickness and also to quantify entrainment.

7. Cloud variability

In this section we study how the shell properties depend on the initial thermodynamic properties of the cloud by studying the results from the different simulations and hence link the internal scales with external flow parameters. A comparison of the shell formation during the first $100s$ for different clouds is shown in figure 9. In simulations (a) A06, (b) A01, (c) A03 and (d) A02, there is an early onset of the buoyancy phase in the shell compared to simulations (e) A05, (f) A04 and (g) A10. In (h) A09 and (i) A07, the drag phase dominates till the end of the simulation. In simulation A08 (not shown) no shell is formed at all.

The mean buoyancy and vertical velocity are analyzed next. Figure 10 shows the normalized plots for $\overline{b}$ and $\overline{w}$. All the selected simulations reach a self-similar regime for buoyancy where $\overline{b}$ collapses neatly in the region where the shell is formed. The collapse for $\overline{w}$ is much less convincing, however, which is expected due to the passive nature of the mean velocity and the ballistic acceleration of the shell.

There is a distinct difference visually in the shell thickness between the different simulations as shown in figure 9. This can be explained by analyzing the budget for the buoyancy flux B given in equation 13. In equation 13, $\frac{dB}{dt}$, is by definition, the rate of growth of the turbulent length scale (or the shell thickness) which is successfully parameterized using b_c and w_c in equation 14. Therefore we have reason to believe that the higher growth rate of the shell thickness could be linked to the higher value of q_l in the cloud which can lead to a higher latent heat release during evaporation; and also the higher initial value of buoyancy b_c in the cloud core, resulting in a much larger horizontal buoyancy gradient at the cloud edge.

The different simulations confirm that the buoyancy scale b^* is indeed the fundamental characteristic scale. Since the shell accelerates ballistically, it follows that a possible relation linking the internal velocity scale with external flow parameters would be $w_{\min} = b^*t$. The higher the magnitude of b^*, the lesser the time needed by the shell to descend. This relationship between $\overline{w}_{\min}$ and b^*t is checked for the simulations in which we see the formation of a subsiding shell and is shown in figure 11. Simulation A10 has been excluded in the figure even though a subsiding shell is generated. This is because the evaporative cooling is not strong enough to generate a negative vertical velocity comparable in magnitude to the $w_{\min}$ seen in the other simulations during the duration of the simulation. We observe a very good relationship between the two quantities (with a slope of approximately 0.15) which leads to the equation

$$\overline{w}_{\min} = 0.25\ |b_s|(t - t_B), \tag{15}$$

where t_B is the time at which the buoyancy phase starts (which is different for each of the simulations considered in figure 11; however no exact relation between t_B and initial cloud thermodynamics was observed using the DNS data).

The time dependence in equation 15 can be removed by using equations 8 and 14, thereby successfully linking the internal velocity scale with the external flow parameters,

$$\overline{w}_{\min} = 0.25|b_s|\left(\frac{|b_s|l^*}{\gamma w_c b_c} - t_B\right). \tag{16}$$

Shell thickness and entrainment

In this sub-section, we develop a model to study the rate of entrainment of the environment air into the cloud. The shell can be considered to be part of the cloud and it grows with the entrainment and mixing with the environment air. Hence turbulent entrainment can be studied in terms of the rate of growth of the thickness l^* of the shell. Comparisons between the observed shell thickness l_s for the different simulations is done in figure 12 where l_s is normalized with the characteristic scale l^* for each simulation. In section 5, a relation $l_s = 2.2l^*$ was observed for simulation A01. Interestingly, this relation holds for all simulations as seen

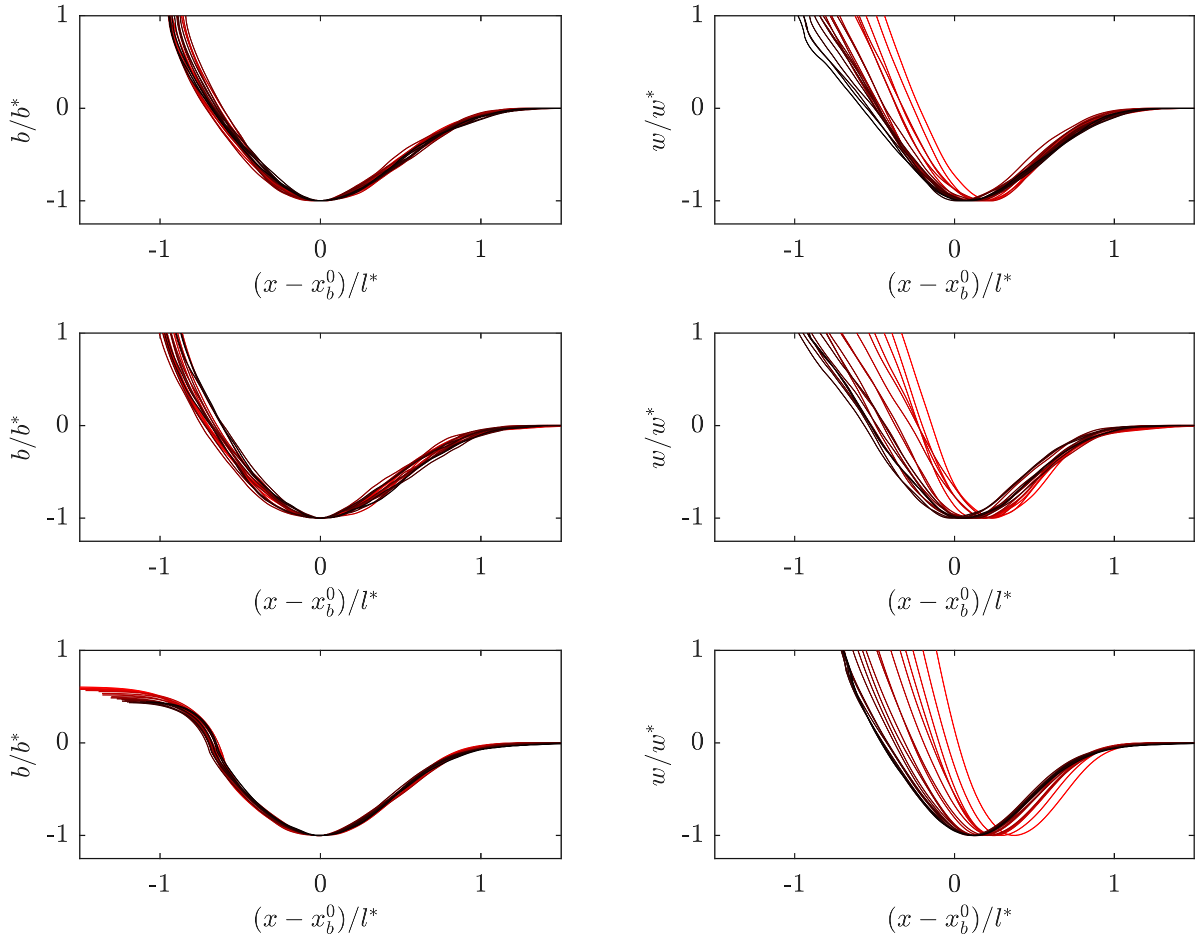

FIG. 10. Self similarity plots for $\overline{b}$ and $\overline{w}$ for different simulations. (a),(b) A01; (c),(d) A02; (e),(f) A06.

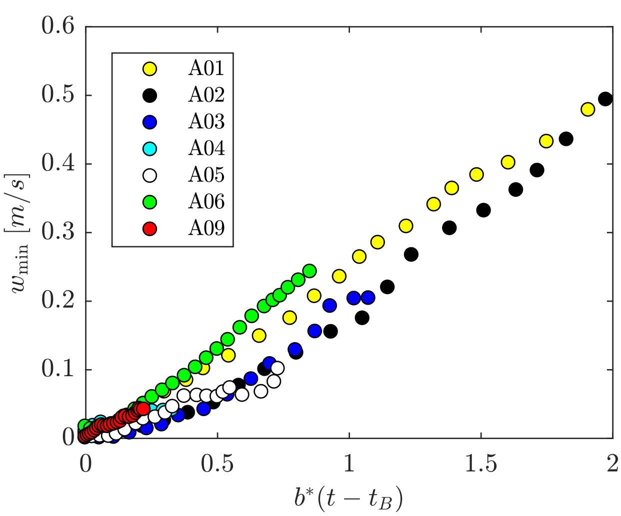

FIG. 11. Relationship between $\overline{w}_{\min}$ and $b^*(t - t_B)$ in a subsiding shell

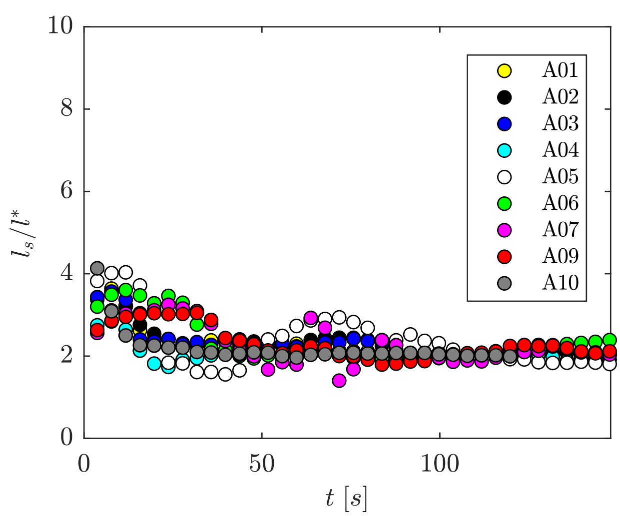

FIG. 12. Evolution of normalized shell thickness.

in figure 12 and be useful in predicting the size of the shell thickness at a particular time given the initial cloud properties.

From this relation, an entrainment analysis can be performed by comparison with the Morton, Taylor and Turner model (Morton et al. 1956) for the turbulent entrainment velocity which is,

$$w_e = \alpha \hat{w} \tag{17}$$

where w_e is the entrainment velocity, which is a fraction of a turbulent characteristic velocity $\hat{w}$. α is the entrainment coefficient. This entrainment hypothesis is the standard closure used in integral descriptions of turbulent flows like jets and plumes (van Reeuwijk and Craske 2015). We adapt this model to be used as a measure of entrainment in our current study. The model connects the velocity at which the environmental air is entrained into the shell (w_e), to a characteristic cloud velocity ($\hat{w}$), by a coefficient of proportionality α.

Considering the entrainment velocity w_e as the rate of change of the characteristic thickness l^* with time, we get,

$$\frac{\mathrm{d}}{\mathrm{dt}}(l^*) = \alpha \hat{w} \tag{18}$$

Using equations 8, 14, and the relation $B \approx \overline{u'b'}|_{x_b^-} t$, l^* can be replaced in equation 18. Comparing the resulting relation with equation 17, the entrainment co-efficient α is given by,

$$\alpha = \frac{\gamma b_c}{|b_s|} \tag{19}$$

The coefficient is constant by definition and the values are given in table 2. The second column indicates whether a subsiding shell is formed within the first 100s of the simulation. The entrainment co-efficient is different for different simulations and shows that entrainment is dependent on the initial thermodynamics and updraft velocities of the cloud and environment.

The entrainment coefficient α can be linked to the fractional entrainment rate ε used in cumulus parameterization schemes for large scale models. This fractional entrainment rate which can be expressed as the ratio of the entrainment rate E to the convective mass flux M is inversely proportional to the radius R of a cloud , i.e. $\varepsilon = E/M \approx \eta/R$, where η is a dimensionless proportionality constant (Squires and Turner 1962; Simpson and Wiggert 1969; Simpson 1971). Assuming a circular cross-section for the cloud,

$$\frac{\eta}{R} = \frac{E}{M} = \frac{2\pi R w_e}{\pi R^2 \hat{w}} \tag{20}$$

Using equation 17 this can be rewritten as,

$$\varepsilon = \frac{\eta}{R} = 2\frac{\alpha}{R} \tag{21}$$

TABLE 2. Parameterization coefficients for all simulations.

Sim No	Shell	b_c	w_c	$F(m^2/s^3)$	γ	$\alpha \approx \eta/2$
A01	Yes	0.039	0.81	2.8 x 10^{-3}	0.09	0.14
A02	Yes	0.057	0.96	3.6 x 10^{-3}	0.07	0.12
A03	Yes	0.046	0.81	2.4 x 10^{-3}	0.06	0.17
A04	Yes	0.042	0.67	1.3 x 10^{-3}	0.05	0.26
A05	Yes	0.072	0.52	2.3 x 10^{-3}	0.06	0.5
A06	Yes	0.004	0.31	2.7 x 10^{-4}	0.22	0.1
A07	No	0.015	0.31	1.9 x 10^{-4}	0.04	0.26
A08	No	0.051	2.03	1.5 x 10^{-4}	0.001	0.31
A09	No	0.011	0.43	2.1 x 10^{-4}	0.04	0.20
A10	Yes	0.001	2.00	2.5 x 10^{-5}	0.01	0.002

Since our temporal simulations do not include a valid cloud radius, a fair comparison with numerical values of ε present in LES studies such as Siebesma and Cuijpers (1995), Dawe and Austin (2011),Romps (2010) is not possible. However, the value of the proportionality constant η can be compared.

For the study in Romps (2010), $\eta/R = (\varepsilon - \delta)/R$, and the values calculated for a cloud layer between 750m and 1400m are, ε = 2.2 km^{-1} to 2.8 km^{-1} and δ = 3.5 km^{-1} to 4.1 km^{-1} resulting in values of $\eta/R = 1.3$. Assuming a radius $R = 500$m, this leads to $\eta = 0.65$. For the current study, $\eta = 2\alpha$ as shown in equation 21, giving numerical values in the range 0.2 to 0.99 which are comparable with that in Romps (2010).

8. Concluding remarks

A numerical case was developed to study the dynamics of the descending shell formed at the edges of actively growing shallow cumulus clouds. DNS was used to conduct a temporal study on the cloud-environment mixing and study the properties of the turbulent flow generated by evaporative cooling. A forcing was applied on the cloud layer to maintain the in-cloud velocity and thermodynamics at pre-defined values to simulate an actively growing cloud. This introduces shear into the setup, and we end up with a buoyantly driven shell inside a shear layer. A bulk condensation scheme was used to describe cloud thermodynamics by diagnostically calculating the liquid water content in the cloud.

Two distinct flow phases were observed within a negatively buoyant turbulent cloud-environment mixture. The first is a 'drag' phase where the momentum flux transfer dominates and the negatively buoyant shell is dragged vertically upwards by the active cloud layer. The onset of the second 'buoyancy' phase occurs when the buoyancy flux within the shell dominates and consequently the shell starts descending. The time at which the onset of the buoyancy phase occurs (leading to the subsequent descending motion of the shell), depends on the dominating term in the velocity flux budget. Higher the momentum flux transfer between the cloud core and the shell, the greater the delay in the onset of the buoyancy phase.

The shell buoyancy scale is observed to be invariant with time which is consistent with what is seen by Abma et al. (2013), and in our case is set entirely by the initial thermodynamic state of the cloud and the environment. However the shell thickness is observed to increase linearly with time while Abma et al. (2013) observed a quadratic growth. Since the rate of change of the shell thickness has been shown to be dependent on the buoyancy flux pumped into the shell at the inner boundary ($\overline{u'b'}|_{x_b^-}$), the addition of positive buoyancy and updrafts in the cloud layer in this study could be the reason for this difference. The presence of the actively growing cloud inhibits the free growth of the shell. The velocity increases ballistically with the acceleration defined by the saturation buoyancy value b_s. The mean velocity is expected to be passive and the turbulent shell is buoyancy driven. Initial cloud conditions like the liquid water content, buoyancy of cloud core, strength of the core updraft etc. define the thickness and growth of the shell.

A self-similar regime is observed after an initial transient. However contrary to classical self similar flows, the TKE budget terms and the velocity moments scale according to the buoyancy and not with the mean velocity. The TKE terms scale with $b^*\sqrt{b^*l^*}$ and the velocity moments with b^*l^*. Internal scales based on the integral quantities of mean buoyancy and vertical velocity were used to show self-similarity. These scales were successfully linked with external flow parameters.

The entrainment coefficient can be calculated by considering the shell as centred on the cloud edge and using the time rate of change of the shell thickness as an entrainment velocity. This coefficient will be a constant for a particular initial state of the cloud and the environment. A comparison is made with parameterization schemes used in large scale models and the numerical values of the entrainment coefficients are found to be of the same order of magnitude.

It is interesting to note here that for this case the shell thickness and the velocity continues to grow indefinitely. Since the shell is in the vicinity of an actively growing cloud, it is continuously fed with moisture from the cloud and the water droplets can evaporate leading to evaporative cooling and further fuelling the shell growth. In the presence of a more mature cloud nearing the end of its lifetime, the shell would have probably grown inward at the expense of the cloud. This could mean that the shell thickness and velocity are limited only by the cloud evolution phase and ultimately lifetime. It is also important to highlight the fact that by imposing a periodic boundary condition on a domain size of $30m$, larger eddies which could dominate flow before the end of the simulation are being suppressed. However due to the limitations of DNS and the temporal setup of the problem, this is unavoidable.

Using relations to predict the thickness and minimum vertical velocity of the shell in a standard shallow cumulus cloud like in simulation A01, the shell thickness would grow to $l_s = 99.8$m considering a cloud updraft lifetime of 408s. The minimum magnitude of the vertical velocity in the shell would reach values of $w_{\min} = -2.3m/s$. This is consistent with values observed in single cloud transects in Katzwinkel et al. (2014). The current experiment was considered with a non-stratified environment, but a stratification in the environment could also possibly limit the velocity and thickness of the shell.

Acknowledgments. Computational resources from an Archer Leadership Grant and Imperial College HPC services are gratefully acknowledged. V. Nair also acknowledges funding from the Marie-Sklodowska Curie Actions under the European Union's Horizon 2020 research and innovation programme (Grant no 675675).

Thijs Heus was supported by the U.S. Department of Energys Atmospheric System Research, an Office of Science, Office of Biological and Environmental Research program, under Grant DE-SC0017999.

APPENDIX

Sensitivity to forcing parameters

The case-setup presented in this work is unique due to the introduction of the volumetric nudging inside the cloud layer. This was done primarily to prevent the shell layer from exhausting the cloud layer which then leads to a very transient flow. However, forcing the cloud layer can have several effects on the flow, primarily with respect to how fast the shell grows or thickens. We perform an analysis to study the sensitivity of the results to the forcing in the cloud layer. This is done by varying the length of the cloud layer (and hence the length over which the forcing is applied), and by changing the time scale of forcing. Two extra simulations B01 and B02 are performed; in B01, τ the time scale of nudging is relaxed, and in B02, L_c the width of the cloud layer is changed. The new simulations are similar in all other parameters to simulation A03.

a. Effect of time scale τ

In simulation B01, L_c is fixed and τ is relaxed to twice the value used in A03, i.e. $\tau = \frac{2L_c}{w_c}$. This results in a softening of the sharp step change in the velocity and the thermodynamic properties, resulting in a shear layer which is much reduced in intensity compared to that in simulation A03 as shown in figure A1 (a) and (b). An analysis of the length scale l^* for B01 clearly shows that the length

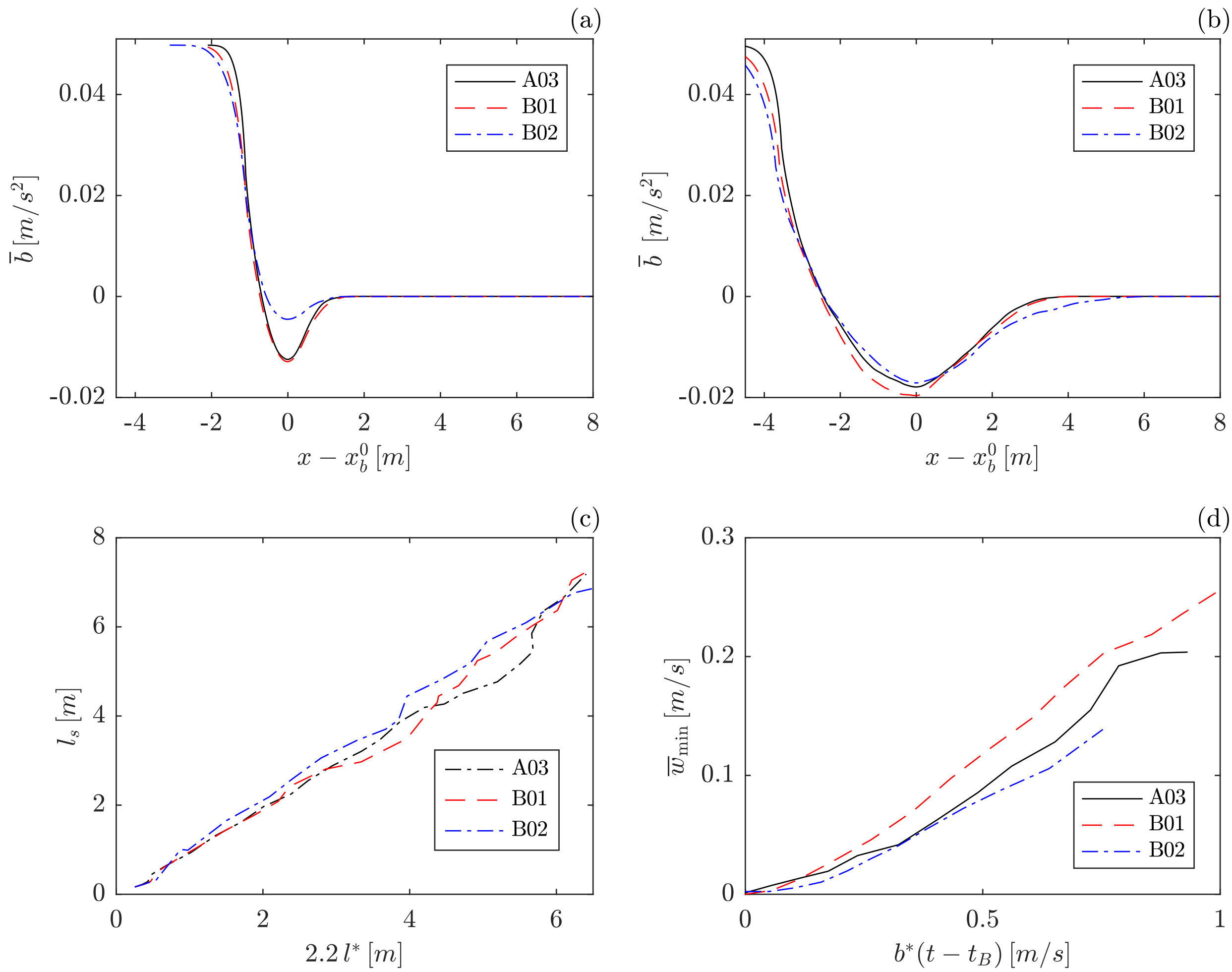

FIG. A1. Mean buoyancy profiles for simulations (a) A03 ($L_c = 1m$), (b) B01 $\left(\tau = \frac{2L_c}{w_c}\right)$, and (c) B02, ($L_c = 2m$)

scale is still increasing linearly with time as shown in figure A1(c). Additionally, figures A1(c) and (d) show that the relations $l_s = 2.2l^*$ and $\overline{w}_{\min} = 0.25\,b^*(t - t_B)$ observed in section 5 holds for B01 as well. This allows us to conclude that the growth of the shell thickness remains unaffected by the intensity of the shear layer at the cloud boundary.

b. Effect of cloud thickness L_c

In simulation B02, τ is fixed and the thickness of the cloud layer is doubled, i.e. $L_c = 2m$. This increases the distance between the left boundary and the shell as shown in figure A1(c). In A03, since the shell forms around $2m$ from the left boundary, turbulent eddies of scales greater than $2m$ will be inhibited by the left boundary. By increasing the width of the cloud layer, eddies of larger scales are also allowed to develop. However, the presence of these larger eddies do not have an effect on the length scale of the shell l^* as shown in figure A1(c). This also highlights the fact that entrainment is dominated by the small scale mixing and could also be an explanation for the agreement between the entrainment coefficients in this DNS study and the LES study in Romps (2010) (which also includes much larger scales of turbulent motion). The relations for l^* and $\overline{w}_{min}$ hold for this case setup as well.

References

Abma, D., T. Heus, and J. Mellado, 2013: Direct Numerical Simulation of evaporative cooling at the lateral boundary of shallow cumulus clouds. *Journal of the Atmospheric Sciences*, **70**, doi: 10.1175/JAS-D-12-0230.1.

Craske, J., and M. van Reeuwijk, 2015: Energy dispersion in turbulent jets. part 1. Direct simulation of steady and unsteady jets. *Journal of Fluid Mechanics*, **763**, 500537, doi:10.1017/jfm.2014.640.

Dawe, J., and P. Austin, 2011: The influence of the cloud shell on tracer budget measurements of LES cloud entrainment. *Journal of the Atmospheric Sciences*, **68**, 2909–2920, doi:10.1175/2011JAS3658.1.

de Rooy, W., and Coauthors, 2011: Entrainment and detrainment in cumulus convection: an overview. *Quarterly Journal of the Royal Meteorological Society*, **00**, 2–29.

Hannah, W. M., 2017: Entrainment versus dilution in tropical deep convection. *Journal of the Atmospheric Sciences*, **74 (11)**, 3725–3747, doi:10.1175/JAS-D-16-0169.1, URL https://doi.org/10.1175/JAS-D-16-0169.1.

Heus, T., and H. Jonker, 2008: Subsiding shells around shallow cumulus clouds. *Journal of the Atmospheric Sciences*, **65**, 1003–1018, doi:10.1175/2007JAS2322.1.

Heus, T., C. Pols, H. Jonker, H. van den Akker, and D. Lenschow, 2009: Observational validation of the compensating mass flux through the shell around cumulus clouds. *Quarterly Journal of the Royal Meteorological Society*, **135**, 101–112.

Heus, T., G. van Dijk, H. Jonker, and H. van den Akker, 2008: Mixing in shallow cumulus clouds studied by lagrangian particle tracking. *Journal of the Atmospheric Sciences*, **65**, 2581–2597.

Hill, M., 1894: On a spherical vortex. *Philosophical Transactions of the Royal Society*, **185**, 213–245.

Jonas, P., 1990: Observations of cumulus cloud entrainment. *Atmospheric Research*, **25**, 105–127, doi:016-8095/90.

Jonker, H., T. Heus, and P. Sullivan, 2008: A refined view of vertical mass transport by cumulus convection. *Geophysical Research Letters*, **35**, L07 810, doi:10.1029/2007GL032606.

Katzwinkel, J., H. Siebert, T. Heus, and R. Shaw, 2014: Measurements of turbulent mixing and subsiding shells in trade wind cumuli. *Journal of the Atmospheric Sciences*, **71**, 2810–2822, doi:10.1175/JAS-D-13-0222.1.

Morton, B., G. Taylor, and J. Turner, 1956: Turbulent gravitational convection from maintained and instantaneous sources. *Proceedings of the Royal Society London A*, **234**, 1–23.

Neggers, R. A. J., 2015: Exploring bin-macrophysics models for moist convective transport and clouds. *J. Adv. Model. Earth Syst.*, n/a–n/a, doi:http://dx.doi.org/10.1002/2015MS000502.

Neggers, R. A. J., M. Khler, and A. C. M. Beljaars, 2009: A dual mass flux framework for boundary layer convection. part i: Transport. *Journal of the Atmospheric Sciences*, **66 (6)**, 1465–1487, doi:10.1175/2008JAS2635.1.

Park, S., P. Gentine, K. Schneider, and M. Farge, 2016: Coherent structures in the boundary and cloud layers: Role of updrafts, subsiding shells, and environmental subsidence. *Journal of the Atmospheric Sciences*, **73**, 1789–1814.

Park, S.-B., T. Heus, and P. Gentine, 2017: Role of convective mixing and evaporative cooling in shallow convection. *Journal of Geophysical Research:Atmospheres*, **122**, 5351–5363, doi:10.1002/2017JD026466.

Perrin, V., and H. Jonker, 2015: Lagrangian droplet dynamics in the subsiding shell of a cloud using Direct Numerical Simulations. *Journal of the Atmospheric Sciences*, **72**, 4015–4028, doi:10.1175/JAS-D-15-0045.1.

Rodts, S., P. Duynkerke, and H. Jonker, 2003: Size distributions and dynamical properties of shallow cumulus clouds from aircraft observations and satellite data. *Journal of the Atmospheric Sciences*, **60**, 1895–1912.

Romps, D., 2010: A direct measure of entrainment. *Journal of the Atmospheric Sciences*, **67**, 1908–1927, doi:10.1175/2010JAS3371.1.

Sherwood, S., D. Hernandez-Deckers, and M. Colin, 2013: Slippery thermals and the cumulus entrainment paradox. *Journal of the Atmospheric Sciences*, **70**, 2426–2442.

Siebesma, A., and Coauthors, 2003: A Large Eddy Simulation intercomparison study of shallow cumulus convection. *Journal of the Atmospheric Sciences*, **60**, 1201–1219.

Siebesma, A. P., and J. W. M. Cuijpers, 1995: Evaluation of parametric assumptions for shallow cumulus convection. *Journal of the Atmospheric Sciences*, **52 (6)**, 650–666, doi:10.1175/1520-0469(1995)052⟨0650:EOPAFS⟩2.0.CO;2.

Simpson, J., 1971: On cumulus entrainment and one-dimensional models. *Journal of the Atmospheric Sciences*, **28 (3)**, 449–455, doi:10.1175/1520-0469(1971)028⟨0449:OCEAOD⟩2.0.CO;2, URL https://doi.org/10.1175/1520-0469(1971)028⟨0449:OCEAOD⟩2.0.CO;2, https://doi.org/10.1175/1520-0469(1971)028⟨0449:OCEAOD⟩2.0.CO;2.

Simpson, J., and V. Wiggert, 1969: Models of precipitating cumulus towers. *Monthly Weather Review*, **97 (7)**, 471–489, doi:10.1175/1520-0493(1969)097⟨0471:MOPCT⟩2.3.CO;2, URL https://doi.org/10.1175/1520-0493(1969)097⟨0471:MOPCT⟩2.3.CO;2, https://doi.org/10.1175/1520-0493(1969)097⟨0471:MOPCT⟩2.3.CO;2.

Sommeria, G., and J. Deardorff, 1976: Subgrid-scale condensation in models of nonprecipitating clouds. *Journal of the Atmospheric Sciences*, **34**, 344–346.

Squires, P., and J. S. Turner, 1962: An entraining jet model for cumulo-nimbus updraughts. *Tellus*, **14 (4)**, 422–434, doi:10.1111/j.2153-3490.1962.tb01355.x, URL https://onlinelibrary.wiley.com/doi/abs/10.1111/j.2153-3490.1962.tb01355.x, https://onlinelibrary.wiley.com/doi/pdf/10.1111/j.2153-3490.1962.tb01355.x.

Taylor, G., and M. Baker, 1991: Entrainment and detrainment in cumulus clouds. *Journal of the Atmospheric Sciences*, **48**, 112–121.

Tiedtke, M., 1989: A comprehensive mass flux scheme for cumulus parameterization in large-scale models. *Mon. Wea. Rev.*, **177**, 1779–1800, doi:10.1175/1520-0493(1989)117.

van Reeuwijk, M., and J. Craske, 2015: Energy-consistent entrainment relations for jets and plumes. *Journal of Fluid Mechanics*, **782**, 333–355.

van Reeuwijk, M., D. Krug, and M. Holzner, 2018: Small-scale entrainment in inclined gravity currents. *Environmental Fluid Mechanics*, **18 (1)**, 225–239, doi:10.1007/s10652-017-9514-3.

Wang, Y., B. Geerts, and J.French, 2009: Dynamics of the cumulus cloud margin: An observational study. *Journal of the Atmospheric Sciences*, **66**, 3660–3677.